JACS
JOURNAL OF THE AMERICAN CHEMICAL SOCIETY

Article

Insight into Design of Improved Oxide Ion Conductors: Dynamics and Conduction Mechanisms in the $Bi_4V_2O_{11}$ Solid Electrolyte

Joseph R. Peet, Chloe A. Fuller, Bernhard Frick, Michael Marek Koza, Mark R. Johnson, Andrea Piovano, and Ivana Radosavljevic Evans

J. Am. Chem. Soc., **Just Accepted Manuscript** • DOI: 10.1021/jacs.9b03743 • Publication Date (Web): 02 Jun 2019

Just Accepted

is published by the American Chemical Society. 1155 Sixteenth Street N.W., Washington, DC 20036

Insight into Design of Improved Oxide Ion Conductors: Dynamics and Conduction Mechanisms in the $Bi_{0.913}V_{0.087}O_{1.587}$ Solid Electrolyte

Joseph R. Peet [a, b], Chloe A. Fuller [a, b], Bernhard Frick [b], Michael M. Koza [b], Mark R. Johnson [b], Andrea Piovano [b*] and Ivana Radosavljevic Evans [a*]

[a] Durham University, Department of Chemistry, Science Site, South Road, Durham, DH1 3LE, UK

[b] Institut Laue Langevin, 71 Avenue des Martyrs, 38000 Grenoble, France

KEYWORDS. Functional oxides; fast ion conductors; ab-initio molecular dynamics; quasielastic neutron scattering;

ABSTRACT: Extensive quasielastic neutron scattering measurements have been used to directly observe oxide ion dynamics on the nanosecond timescale in bismuth vanadate with formula $Bi_{0.913}V_{0.087}O_{1.587}$, which exhibits remarkable oxide ion conductivity at low temperatures. This is the longest timescale neutron scattering study of any fluorite-type solid electrolyte and it represents only the second case of oxide ion dynamics in any material observed on a nanosecond timescale by quasielastic neutron scattering. *Ab initio* molecular dynamics simulations reveal two mechanisms that contribute to the oxide ion dynamics in the material: a slower diffusion process through the Bi-O sublattice and a faster process which corresponds to more localised dynamics of the oxide ions within the VO_x coordination spheres. The length of the trajectories simulated and the validation of the simulations by neutron scattering experiments provide for the first time a quantitative insight into the relative contributions of the two processes to the oxide ion conduction in this exceptional solid electrolyte, which can be used to derive design principles for the preparation of related oxide ion conductors with even better properties.

Introduction

Oxide ion conductors are important and technologically exploitable materials used in several types of devices for energy-related and environmental applications. These include oxygen sensors and pumps, dense membranes for oxygen permeation and solid oxide fuel cells (SOFCs).[1,2,3,4] The optimisation of materials for different applications involves improving the oxide ion conductivity at device-operating temperatures, and for SOFCs a conductivity of at least 10^{-2} S/cm is typically sought.[5,6]

The remarkable properties of bismuth vanadate with formula $Bi_{0.913}V_{0.087}O_{1.587}$ were first reported by Kuang *et al.*[7], who reported that this material had the highest oxide ion conductivity of any stable doped-Bi_2O_3 phase, namely 3.9×10^{-2} Scm^{-1} at 500 °C. Importantly, the material was found to adopt a pseudo-cubic long-range ordered fluorite-type 3×3×3 superstructure, imparting stability with respect to transformation to a lower-symmetry lower-conductivity phase. The room temperature structure can be described as consisting of two sublattices. The first of these is made up of isolated VO_4 tetrahedra, with V^{5+} centres separated from each other by around 6.7 Å; this will be referred to as the V-O sublattice. The bulk of the material is made up of a network of corner and edge-sharing OBi_4 tetrahedra with intrinsic oxide vacancies similar to δ-Bi_2O_3, which will be referred to as the Bi-O sublattice. Kuang *et al.*[7] also reported preliminary *ab initio* molecular dynamics (AIMD) calculations carried out for 20 ps of simulation time. These relatively short simulations only provided qualitative insight but suggested that oxide ion dynamics in $Bi_{0.913}V_{0.087}O_{1.587}$ involved vacancy hopping through the Bi-O sublattice and oxide ion exchanges between the two sublattices. The latter cause an increase in the average V coordination number and create additional vacancies within the Bi-O sublattice. The very high conductivity in $Bi_{0.913}V_{0.087}O_{1.587}$ was attributed to three factors: the extended δ-Bi_2O_3-like Bi-O sublattice, the ability of V^{5+} to support variable coordination number (i.e. the existence of VO_x groups at higher temperatures), and the oxide ions readily undergoing localised motion within the VO_x groups.[7]

AIMD simulations have only been reported for a few Bi_2O_3 based solid electrolytes. A slightly more highly V-doped phase $Bi_{0.852}V_{0.148}O_{1.648}$ was found to have lower conductivity,[8] attributed to a larger number of VO_4 groups disrupting the 3-dimensional connectivity of the Bi-O sublattice and the resulting symmetry lowering to monoclinic. Bismuth molybdate with formula $Bi_{0.722}Mo_{0.278}O_{1.917}$ ($Bi_{26}Mo_{10}O_{69}$)[9] has a different structure, made up of columns of δ-Bi_2O_3-like regions surrounded by connected

MoO_x groups. Simulations showed a much larger conductivity contribution from the MoO_x groups, with a "zig-zag" mechanism between the edges of the Bi_2O_3 columns. Bismuth rhenate $Bi_{0.933}Re_{0.066}O_{1.633}$ ($Bi_{28}Re_2O_{49}$)[10] has a structure made up of isolated ReO_x polyhedra dispersed in a Bi-O sublattice, and AIMD simulations on this material showed similar conduction pathways as those described qualitatively for $Bi_{0.913}V_{0.087}O_{1.587}$. Finally, the case of $Bi_{0.9375}Nb_{0.0625}O_{1.5625}$[11] is somewhat different as the Nb atoms are statistically distributed across the Bi sites rather than forming a separate sublattice. The mechanism found in AIMD calculations was vacancy-hopping through the δ-Bi_2O_3-like structure, with no additional processes observed.

Quasielastic neutron scattering (QENS) is a powerful probe of dynamics in different classes of materials, including soft matter and biologically-relevant systems. [12] It is a technique highly suitable to study the diffusion phenomena and over the years it has contributed significantly to the microscopic understanding of solid state diffusion. The QENS signal is observed as broadening of the elastic line in the neutron scattering spectrum, which occurs due to small energy exchanges between the neutrons and the sample during stochastic motion processes in the material. One of the key advantages of QENS is the ability, at least in principle, to distinguish between the long-range diffusion and confined, localised dynamics. Quantitative parameters, including activation energies, diffusion jump lengths and lifetimes, can be obtained from data collected as a function of temperature. QENS has been applied very extensively and successfully to the studies of proton conductors [13], owing to the large incoherent neutron scattering cross section of hydrogen that makes the self-diffusion information readily accessible and ensures that strong signals can be observed from samples containing relatively few protons or those which exhibit relatively low proton mobility. By contrast, oxygen is an essentially pure coherent neutron scatterer, rendering the relevant self-diffusion information more difficult to extract, which has historically limited the use of QENS in the studies of oxide ion conductors. Only recently, with the increased performances of modern instruments in term of incident flux and detection efficiency as well as access to longer diffusion timescales up to nanoseconds, studies of diffusion in oxygen ions conductors can be more readily performed.

Attempts to experimentally probe the microscopic mechanism behind oxide ion conduction in Bi_2O_3-based materials and to quantitatively characterise it through AIMD simulations are scarce. The first study of δ-Bi_2O_3 carried out by Mamontov provided evidence for long-range oxide ion diffusion in the form of a quasielastic neutron scattering (QENS) signal.[14] This study found jump distances of 2.64-2.84 Å (at various temperatures), in excellent agreement with the 2.83 Å distance between the nearest-neighbour oxide ion sites in the <100> direction in δ-Bi_2O_3, thus matching the believed conductivity pathway. Another study of δ-Bi_2O_3, reported by Wind *et al.*,[15] also reported a QENS signal caused by long-range oxide ion diffusion. Using an analysis procedure different to that employed by Mamontov, a jump distance of 3.33 Å was found. This value is larger than the 2.83 Å distance between the nearest-neighbour oxygen sites along <100>, and it was explained by proposing that jumps could occur in other directions, including <110> and <111>, with the distance of 3.33 Å being the weighted average over all these possible jumps.

Building on separate computational and experimental studies, our recent work has demonstrated that combining AIMD simulations with inelastic neutron scattering (INS) and quasielastic neutron scattering (QENS) spectroscopy can yield significant new atomic-level quantitative insight into ionic mobility in structurally complex solid electrolytes. This combined approach has been used to directly observe and elucidate oxide ion dynamics in $La_2Mo_2O_9$.[16] This study gave the first proof that exchange processes leading to long-range oxide ion diffusion rely on the variability of the coordination number and geometry around the Mo^{6+} cations (as postulated in the earlier crystallographic work[17]), with oxide ions jumps occurring both within and between different Mo coordination spheres. It was also possible to differentiate between the roles of different crystallographic sites, offering the atomic-level understanding of the oxide ion dynamics in $La_2Mo_2O_9$ consistent with the macroscopic experimental observations. Similarly, AIMD simulations supported by neutron scattering experiments elucidated the mechanisms of ionic diffusion in apatite-type Bi(III)-containing germanates, providing a quantitative insight into the anisotropic nature of diffusion in these materials and its dependence on the composition and temperature.[18]

The objective of the work presented here was to investigate the dynamics of oxide ion conduction in $Bi_{0.913}V_{0.087}O_{1.587}$ using the combined AIMD and QENS approach. Neutron scattering experiments were carried out to probe longer (nanosecond) timescales with the goal of observing slower longer-range mobility Additional neutron scattering measurements were carried out to investigate the oxide ion dynamics associated with localised motions on picosecond timescales. *Ab initio* molecular dynamics calculations were carried out at three temperatures and for much longer simulation times than undertaken previously (240 ps *vs* 20 ps).[7] The aim of this combined experimental and computational study was to provide the first quantitative insight into the relative contribution of the different mechanisms to the exceptional conductivity in this material and, from this, to propose design principles for related oxide ion conductors with even better properties.

Experimental

Synthesis

A 10 g sample of $Bi_{0.913}V_{0.087}O_{1.587}$ was synthesised following the literature procedure.[7] The stoichiometric quantities of Bi_2O_3 and V_2O_5 reagents were thoroughly mixed and ground together. The powder was placed in an alumina crucible and fired sequentially at 700, 750, 800 and 850 °C with heating and cooling rates of 5 °C min^{-1}. The sample was heated for 12 hours at each temperature with cooling and grinding in between. Sample purity was confirmed by

laboratory X-ray diffraction (Bruker D8 Advance, Cu Kα radiation, LynxEye detector), using the Rietveld method implemented in TOPAS Academic software. [19-21]

Quasielastic Neutron Scattering (QENS)

Neutron scattering data were collected on time-of-flight spectrometer IN6 and on the backscattering spectrometer IN16B at the Institut Laue Langevin (ILL).

The IN6 experiment was performed with an incident neutron wavelength of 4.1 Å to access quasielastic region with an elastic energy resolution of 170 μeV. This configuration allowed to probe dynamics of tenths of picoseconds. The 10 g sample was placed in a cylindrical Nb sample holder and data were collected at 200, 300, 400, 500, 600, 820 °C with a collection time of 6.5 hours at each temperature. Vanadium sample was also measured at 20 °C for 6 hours for normalisation and to provide the resolution function.

The IN16B experiment, with an incident neutron wavelength of 6.271 Å and an elastic energy resolution of 0.75 μeV, gave access to the nanosecond dynamics. The 10 g powdered sample was placed in a cylindrical Nb sample holder. Measurements of elastic intensity (E = 0 μeV) and inelastic intensity at 2 μeV, were made in temperature scans from 20-500 °C with a heating rate of 0.04 °C s^{-1}. Data points were collected in pairs with elastic intensity (EFWS – elastic fixed window scan) measured for 30 seconds, immediately followed by an inelastic intensity (IFWS – inelastic fixed window scan) measurement lasting 2 minutes.[22] QENS measurements were then performed at 10 temperatures (40, 200, 250, 300, 333, 366, 400, 450, 475, and 500 °C). Data were collected for 6 hours at each temperature within an energy transfer window limited to ±10 μeV in order to gain better statistics. For the same reason and to allow the Q-dependence of the scattering function to be determined, additional data were collected at 400 °C and 450 °C for a total of 18 hours at these temperatures. For the analysis of QENS data, a resolution function from a standard vanadium sample was also acquired. The data from both the IN6 and IN16b neutron scattering experiments were analysed using the LAMP software.[23]

Computational methods

AIMD calculations were carried out using density functional theory (DFT) method implemented in the VASP code.[24] The simulations were performed on a pseudo-cubic 3 × 3 × 3 fluorite supercell of the $Bi_{0.913}V_{0.087}O_{1.587}$ structure. This cell contains 96 Bi and 12 Bi/V sites. To ensure all sites were fully occupied by a single atom, 9 of these shared sites were chosen using a random number generator to be occupied by V and the remaining 3 by Bi. Oxygen sites were assigned randomly to make each V atom four-coordinate and provide a total of 171 oxygens in the supercell. This gives a final formula of $Bi_{99}V_9O_{171}$ which is the closest whole-number formula possible to $Bi_{0.913}V_{0.087}O_{1.587}$ for this size supercell. For all calculations PAW pseudopotentials[25] were used with GGA-PBE functionals[26] and before all other calculations geometry optimisation was carried out. The electronic structure was sampled at the gamma point. A phonon density of states (DOS) was also determined from gamma-point phonons calculated using DFT with the finite displacement method. The AIMD calculations were performed at 200 °C, 400 °C, and 600 °C in the NVT ensemble. A total of 120,000 steps of 2 fs were calculated giving a total of 240 ps of simulation time at each temperature. Mean square displacements were produced using the MDANSE code[27] and cloud plots for trajectory visualisation were produced using LAMP.[23]

Results and Discussion

Direct Observation of Oxide Ion Dynamics

$Bi_{0.913}V_{0.087}O_{1.587}$ shows remarkable oxide ion conductivity in the low-temperature range (300-500°C), as demonstrated by impedance spectroscopy.[7] With the aim of understanding the microscopic origin of this property, we performed quasielastic neutron scattering experiments exploiting the timescales of nanoseconds, in which, with support from our *ab-initio* simulations, we identified long-range oxide ion diffusion processes.

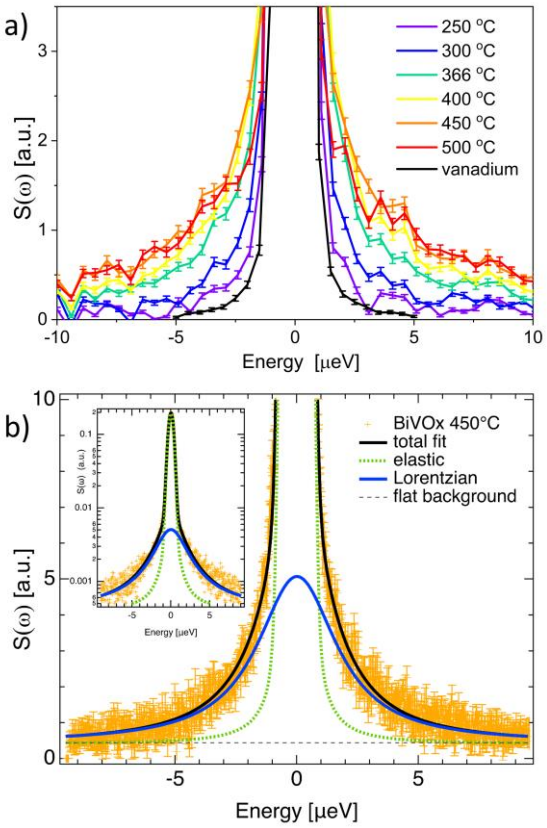

Figure 1. a) $S(\omega)$ spectra for inelastic neutron scattering measurements on $Bi_{0.913}V_{0.087}O_{1.587}$ measured on IN16B at various temperatures with a maximum energy transfer of ±10 μeV. The data hve been summed over all Q. A vanadium resolution function is also shown. b) Representative fit to the IN16B data. The S(ω) of $Bi_{0.913}V_{0.087}O_{1.587}$ at 450 °C, with an evident quasielastic signal. Data have been fitted with a delta function representing the elastic peak and a Lorentzian for the quasielastic peak, both convoluted with the resolution function. A flat background was also used in the fitting.

Plots of the Q-integrated spectra, $S(\omega)$, against energy transfer for 6 out of the 10 temperatures studied on IN16B are shown in Figure 1a (other temperatures have been omitted for clarity), along with a vanadium resolution function. Below 300 °C all spectra are similar to the resolution function with no clear temperature-dependent QENS peak visible; however, from 300 °C a very clear QENS signal appears in addition to the elastic peak. The increasing broadening of the QENS signal indicates that the rapidity of motion is increasing with temperature, and so the evolution of the QENS half-with-at-half maximum (HWHM) linewidth (Γ) was plotted against temperature to allow an activation energy to be calculated.[28]

The $S(\omega)$ data were fitted model-free with a delta function representing the elastic peak and a Lorentzian for the quasielastic peak, both convoluted with the resolution function. A flat background was also used in the fitting (see Figure 1b). in Supporting Information. Temperatures 300 °C and below were omitted due to the low intensity or absent QENS signal. The plot of $\ln(\Gamma)$ against $1000/T$ in Figure 2 gives an activation energy of 0.32(2) eV.

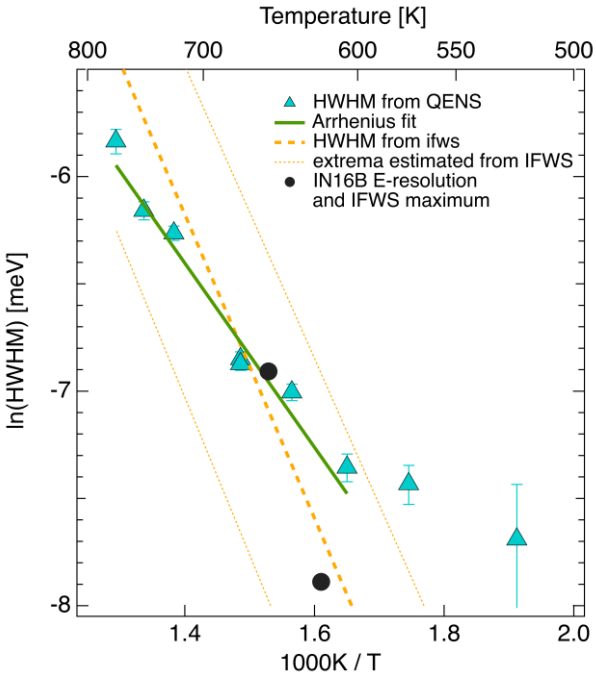

Figure 2. An Arrhenius plot showing the variation of the spectral linewidth Γ with inverse temperature for $Bi_{0.913}V_{0.087}O_{1.587}$ fitted over a 333-500 °C temperature range. The green solid line is the fit to an Arrhenius dependence of the HWHM. The steeper dashed yellow line corresponds to the fit result of the IFWS curves discussed later (dotted yellow lines are calculated from the error bars). The solid black circles are estimated from the IN16B HWHM energy resolution and the onset of the dynamics seen in the EFWS as well as from the temperature of the peak maximum in the IFWS for 2 μeV.

Additional longer data collections on IN16B were performed at 400 °C and 450 °C (temperatures close and at the maximum inelastic intensity, respectively) for a total of 18 hours to achieve sufficiently good statistics to investigate the variation of the scattering function with Q. For these spectra the scattering functions at each Q value were again separately fitted with a Lorentzian (QENS peak) and a delta function (elastic peak) convoluted with the resolution function and a flat background.

For jump diffusive motions, the linewidth Γ of the Lorentzian is expected to follow the Chudley-Elliott model.[28] The fits of this model to the Γ values at 400°C and 450°C are shown in Figure 3. The Q values at which Bragg peaks are present (x = 1.06, 1.38, 1.79 Å^{-2}) are marked by the vertical grey rectangles. In spite of the long measuring time the data are noisy, but the fit curves show that the Chudley-Elliott model is consistent with the data. The calculated lifetime value was about 1 ns; in the fitting of both data sets, the jump length was fixed to 2.83 Å, corresponding to the distance between nearest neighbour oxygen sites. The lifetime value matches well with the timescales probed by IN16B.

An important question is whether the dynamics observed on IN16B is of local or diffusional character. For a translational diffusion model the intensity of the spectral function should remain constant with increasing temperature if the number of scattering particles involved remains constant. In our data, for temperatures where the QENS signal is clearly broader than the resolution function, this type of behavior is observed (333, 366, 400 °C in Figure S1). At the highest temperatures measured we see a decrease of the spectral weight, which can be ascribed to a combined effect of losing part of the signal from the narrow energy window. The typical signature of the translational diffusion probed by QENS is the Q-dependence of the HWHM. Despite a lack of low-Q (< 0.5 Å^{-1}) data points, our data at both 400 and 450 °C exhibit HWHM vs. Q trends consistent with the Chudley-Elliot model, pointing to a translational diffusive nature of the observed dynamics. In addition, the appearance of very clear QENS signals from 300 °C onwards coincides with a gradient change in the Arrhenius curve from the impedance measurements, where the oxide ion conductivity activation energy decreases from 1.1 eV to 0.68 eV.[7] This strongly suggests that the dynamics observed in the neutron scattering experiments described here correspond to the oxide ion conductivity of $Bi_{0.913}V_{0.087}O_{1.587}$ probed by impedance measurements.[7]

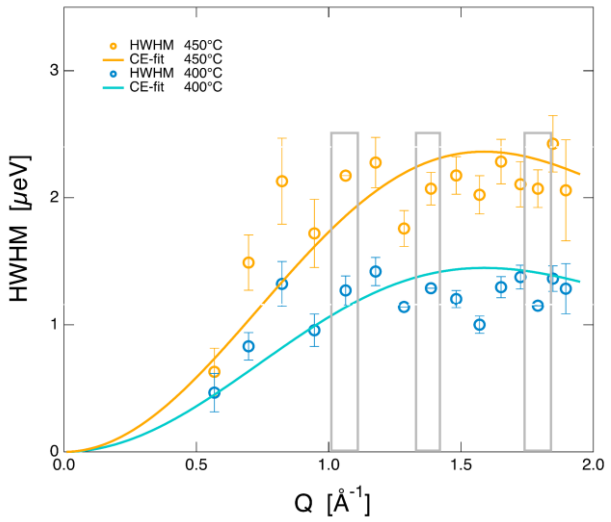

Figure 3. QENS spectral linewidth *HWHM vs Q* for $Bi_{0.913}V_{0.087}O_{1.587}$ at 400°C and 450°C fitted with the Chudley-Elliott model. Grey rectangles correspond to Bragg peak positions.

The IN16B instrument offers additional means of monitoring the elastic and inelastic scattered intensity changes as a function of temperature through short elastic fixed window scan (EFWS) and inelastic fixed window scan (IFWS) measurements. Plots of the Q-integrated and normalised (to the 20°C signal) EFWS and 2 μeV IFWS, collected as a function of temperature, are shown in Figure 4 (light blue triangles and orange points, respectively; note the factor of 10^3 difference in scales).

The IFWS intensity at 2μeV (open circles, lower part of Figure 4) shows a single peak at about 440°C. The decrease of the EFWS intensity between T=20°C and 500°C (light blue triangles, upper curve in Figure 4) appears to take place in two steps. To further evidence this effect we fitted the EFWS intensity with a two-step function as reported in Figure S2 in Supporting Information. The first decay in the elastic intensity happens between 20 and 250°C, with an inflection point at 121°C, and accounts for about 1/3 of the total EFWS intensity loss. This effect is not accompanied by a corresponding increase in the 2μeV IFWS intensity. This indicates that the elastic intensity loss cannot be explained by the formation of a quasielastic peak in the IN16B time-window and instead may originate from different effects: i) Debye-Waller effects (i.e. it is due to thermal motions of the scattering atoms); ii) changes in the elastic coherent (Bragg or diffuse) scattering; iii) transfer to a very broad quasielastic intensity outside the selected time-window, caused by very fast diffusing species contributing only to a small background increase in the measured time window on IN16B.

To determine the possible contribution of effects ii) and iii) to the IN16B data, we performed quasielastic measurements using the time-of-flight spectrometer IN6, with a resolution of 170 μeV, allowing access to a larger Q-range (to probe effect ii) and faster, possibly localised dynamics on the ps timescales (to probe effect iii).

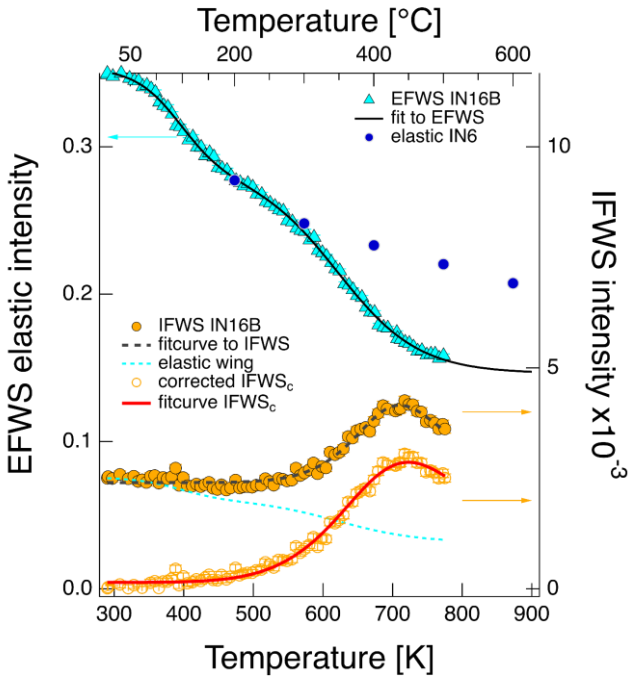

Figure 4. Upper part: Plots of the integrated elastic intensity (EFWS) against temperature for neutron scattering experiments on $Bi_{0.913}V_{0.087}O_{1.587}$ carried out with IN16B (light blue triangles). Also shown is a fit curve for a two-step decay indicating the steepest descents at 121°C and 349°C. The filled blue circles correspond to the integrated elastic intensity measured on IN6, rescaled at 200°C to the IN16B data. Lower part: Plots of the inelastic intensity measured at 2 μeV against temperature (filled yellow circles) and corrected (open circles) for a hypothetical elastic contamination (dashed blue line) showing peak maxima at 436°C and 449°C respectively according to the fits (dashed black and red continuous line).

In the IN6 experiments, we probed the total elastic intensity loss (coherent + incoherent) by integrating $S(Q,\omega)$ on a narrow window around the zero energy transfer, and the total elastic intensity loss without Bragg contributions (incoherent only). The trends of the two data-point sets correspond well (Figure S3 in Supplementary Information), meaning that coherent and incoherent parts contribute equally to the intensity loss and structural modifications of the material alone cannot account for the effect. We can therefore exclude effect ii as the origin of the apparent low-temperature step loss of elastic intensity in EFWS data.

The IN6 data can also be used to evaluate effect iii. We note that the trend of the total elastic intensity deduced from IN6 spectra as a function of temperature (blue filled circles in Figure 4, normalised to the 200 °C temperature to IN16B data) appears to align with the first EFWS decay observed on IN16B. This suggests that with the IN6 energy window it might be possible to detect the second, faster dynamics process, which cannot be observed on IN16B. Indeed our simulations (*vide infra*) suggest that the fast dynamics on the ps timescale are associated with local motions in the V-O sublattice.

The IN6 data collected on $Bi_{0.913}V_{0.087}O_{1.587}$ were therefore analysed further to test this hypothesis. Figure 5 shows the temperature-dependent neutron quasielastic data corrected for the Bose population. Attempts to fit the data, using a delta function for the elastic signal and a Lorentzian broadening for the quasielastic component, both convoluted with instrument resolution, confirmed the absence of a detectable quasielastic signal. The reason could be that this faster dynamics occurs on a different timescale than that probed by the IN6 spectrometer. For example, Wilmer *et al*. showed that in sodium orthophosphate the isolated PO_4 groups underwent reorientation dynamics on the ps timescale.[29,30] In our data, the absence of a quasielastic signal can also be due to the fact that, because of the small scattering cross section of oxygen and a small number of oxide ions undergoing this type of dynamics (*vide infra*), the quasielastic intensity is not detectable in this experiment. In this regard an analysis of the normalised elastic and inelastic (E= -0.7 meV) intensities showed that the loss of elastic and inelastic intensity does not occur at the same rate as a function of temperature, with the inelastic loss being more rapid (Figure S3). This can also indicate that another dynamic process (other than the expected Debye-Waller effect) is already active at 200 °C, although our data do not demonstrate this directly.

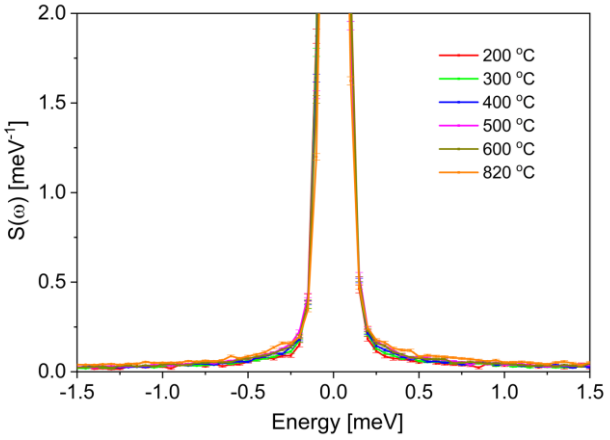

Figure 5. The *Q*-integrated scattering function, $S(\omega)$, against neutron energy transfer at various temperatures for $Bi_{0.913}V_{0.087}O_{1.587}$ measured on IN6, after correction for the Bose population factor.

Coming back to the EFWS of IN16B of figure 4, a second EFWS intensity decrease with increasing temperature becomes evident above 216 °C, with the steepest descent at 349°C. The loss accounts for about 2/3 of the total elastic intensity decrease and is accompanied by a large increase in the 2μeV inelastic intensity with a peak near 437°C. This indicates that from 300 °C there is onset of oxide ion dynamics on the nanosecond timescale window of IN16B, causing the appearance of the QENS signal (Figure 1). The temperature of this effect in the EFWS intensity coincides with the decrease in the activation energy determined by impedance measurements, again strongly suggesting that the same dynamics are being observed. The 2μeV IFWS intensity peak at 437°C indicates that the QENS signal broadens with temperature, that it has reached the maximum intensity at this temperature, and that it is broadening further as the rate of oxide ion mobility increase with temperature; at higher temperatures the broadening starts causing a decrease in IFWS amplitude, due to the fact that signal is going out of the 2μeV energy window. The temperature dependence of the quasielastic intensity in the region close to the elastic line in Figure 1 therefore matches the temperature dependence of IFWS in Figure 4.

The IWFS data can also be used to determine the activation energy for the dynamic process observed. Since we had no clear evidence of a faster process occurring in connection with the first EFWS intensity drop, we treated the IFWS slope in this temperature range as an elastic contamination (leakage) and subtracted the rescaled EFWS intensity from it.[22] This gives an activation energy of 0.46(1) eV.

We conclude, based on the excellent agreement of the onset temperatures, that the observed changes in the QENS and IFWS data capture the same dynamic process, and from the two fitting procedures we can estimate its activation energy as 0.39(4) eV. This is lower than the value of 0.68 eV found by Kuang *et al.* from impedance measurements in this temperature range.[7] This level of difference between the activation energies determined from the impedance measurements and measurements such as QENS, solid state NMR and tracer diffusion measurements, as well as simulations, has been reported in a range of fast ion conductors, *e.g.* for nominally "Na-doped $SrSiO_3$"[31], $La_2Mo_2O_9$[16] and other oxide ion conductors,[32,33] as well as Na^+ ion conductors[34,35] and Li^+ ion conductors.[36,37] Recent studies ascribed this discrepancy between macroscopic and microscopic diffusion to the fact that the activation energy for the former can be affected by ion-ion interaction, while the energy barriers from QENS and simulations correspond to independent oxygen hops.[38,39]

Oxide Ion Dynamics and Conduction Mechanisms Investigated by *Ab Initio* Molecular Dynamics

With the aim to deepen our understanding of the microscopic conduction mechanism and the structure-dynamics relationships in $Bi_{0.913}V_{0.087}O_{1.587}$, we investigated the oxygen mobility using *ab initio* molecular dynamics.

Figure 6a shows the mean square displacement (MSD) of the oxygen atoms at each temperature over the course of the simulation. As expected, the MSDs increase with temperature indicating increased oxide ion motion. There is no evidence of the overall MSD saturating, indicating that the motion is not confined to a fixed volume.

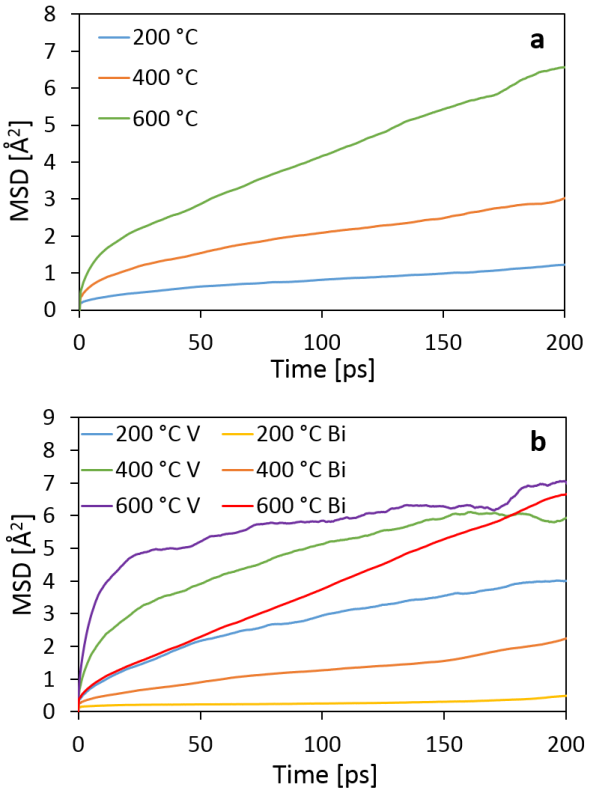

Figure 6. a) Mean square displacements for all oxygen atoms in the simulation box calculated from AIMD simulations at several temperatures. b) Mean square displacements for oxygen atoms starting in the V-O sublattice (V) or part of the Bi-O sublattice (Bi).

Deeper insight into the contribution of the two sublattices to the O^{2-} conduction can be obtained by splitting the MSDs of oxygen atoms in the V-O sublattice and those which are part of the Bi-O sublattice, as shown in Figure 6b. One very interesting finding is that at temperature as low as 200 °C, the MSD of the oxygen atoms bonded to V already shows delocalisation (~ 2Å), suggesting the onset of dynamics that then initially continuously becomes larger with increasing temperature. The fact that the MSDs for the V-O sublattice show a plateau clearly indicate localised diffusion. These results indicate that the initial loss of elastic intensity below 300 °C, which has no clear counterpart in the inelastic fixed window scan (Figure 4) is in part due to the volume-constrained oxide ion dynamics within the V-O sublattice. This conclusion is supported by recent variable temperature multinuclear solid state nuclear magnetic resonance (SS-NMR) study on $Bi_{0.913}V_{0.087}O_{1.587}$, which showed significant rates of tetrahedral VO_4 group rotations even at room temperature.[40] The difference in behaviours of the two sets of oxygen atoms indicates that there are two processes occurring in this material on different timescales: a process which is a key contributor to the long-range diffusion through the Bi-O sublattice (which we could experimentally observe in IN16B QENS data, Figure 4) and a faster process involving oxide ion mobility within individual VO_x groups (which we did not observe in the IN6 data, Figure 5).

Diffusion coefficients, *D*, have been calculated at each temperature by determining the gradients of the MSDs. From the MSDs for all the oxygen atoms the activation energy calculated was 0.17(1) eV (Figure 7a), lower than the 0.39(4) eV value found from QENS and IFWS data. This value is likely largely affected by contributions from the oxygen atoms involved in localised processes within the VO_x groups. A plot of the *D* values calculated only using the MSDs for the Bi-O sublattice O atoms against $1000/T$ (Figure 7b) gives an activation energy of 0.38(1) eV, which is in excellent agreement with 0.39(4) eV from the QENS and IFWS measurements, indicating that the long-range diffusion through the Bi-O sublattice is indeed the dynamic process observed in the IN16B experiments. The activation energy calculated from the MSD curves for the V-O sublattice O atoms is 0.05(1) eV, which is consistent with the observation of very facile localised motion in this sublattice from the SS-NMR experiments, and the activation energy of 0.07(2) eV determined there from the temperature dependence of linewidths. [40] Low-temperature oxygen localised dynamics and low activation energies for the reorientation of the metal-oxygen coordination polyhedra have been reported in different structure types. For example, in the $ZrW_{2-x}Mo_xO_8$ ($0 \le x \le 2$) negative thermal expansion materials, oxygen mobility has been observed at temperatures as low as 200 K, with activation energies of 0.23-0.35 eV for the reorientations of $(W/Mo)O_4^{2-}$ groups which share most corners to form the three-dimensional framework structure.[41-43] Activation energies ranging between 0.05-0.18 eV have been found by QENS for the xNa_2SO_4 $(1-x)Na_3PO_4$ ($0 \le x \le 0.5$) materials which contain isolated tetrahedral groups.[29] Similarly, rapid polyhedral rotations at low temperatures and very low activation barriers have been reported from for isolated MnO_4^- tetrahedra in $KMnO_4$ (E_{act} = 0.07 eV). [44]

In order to obtain quantitative insight into the relative contributions of the two different types of processes occurring in $Bi_{0.913}V_{0.087}O_{1.587}$ over the course of the simulations, the number of diffusion events at each temperature was recorded. For this purpose, a jump was defined as an oxide ion moving a distance of at least 1.5 Å (smaller than the distance between oxygen sites so as not to miss any jumps) within 500 simulations steps. The jumps were grouped into several categories based on the closest cations before and after the jump, and results are shown in Table 1. Intra-VO_x jumps are oxide ion jumps between two sites within a single V atom coordination sphere; this corresponds to the fast process discussed above. Bi-O is a jump within the Bi-O sublattice, either between two different Bi coordination spheres or from one site to another in the same Bi coordination sphere. These were grouped together as the connected nature of the Bi-O sublattice means that each oxygen atom is bonded to four bismuths and so the specific closest Bi is not as meaningful. This corresponds to the slow process mentioned above. Finally, V-Bi and Bi-V represent jumps from the VO_x groups to the Bi-O sublattice and *vice versa*.

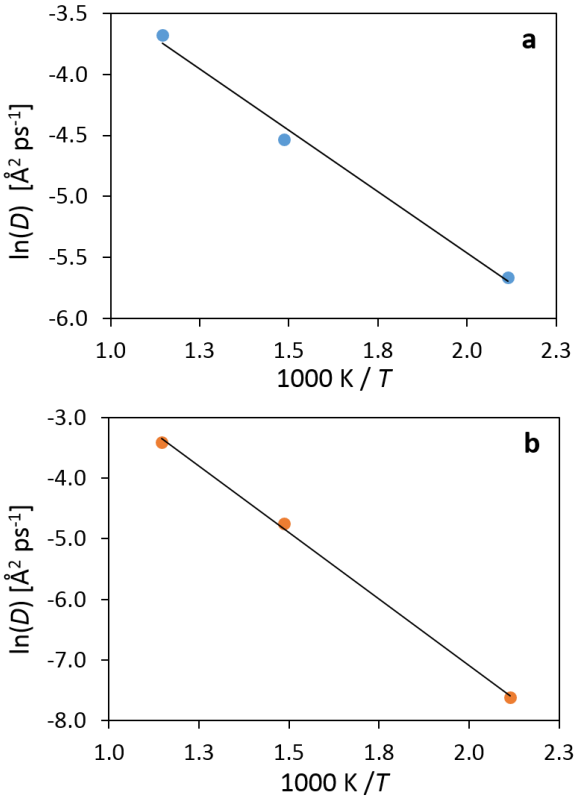

Figure 7. a) Arrhenius plot of diffusion coefficients calculated from the gradients of the MSDs for all oxygen atoms shown in figure 6a. b) Arrhenius plot of diffusion coefficients calculated from the gradients of the MSDs for oxygen atoms beginning as part of the Bi-O sublattice shown in Figure 6b. The size of the error bars are of the order of the size of the data points used.

Table 1. The number and percentage of each type of oxide ion jump described in the text counted over the entire AIMD simulations at each of the three temperatures.

Jump Type	200 °C		400 °C		600 °C	
	#	%	#	%	#	%
Intra-VO_x	339	69.3	863	59.3	1062	55.8
V-Bi	19	3.9	70	4.8	106	5.6
Bi-V	20	4.1	73	5.0	108	5.7
Bi-O	111	22.7	450	30.9	628	32.9
Total	489		1456		1904	

As expected from the MSDs, the number of total jumps, as well as jumps of each type, increases substantially with temperature, with the largest increase being between the 200 and 400 °C simulations. This correlates very well with the activation of dynamics at 300 °C observed in the QENS data and the change in gradient observed in impedance measurements. The number of intra-VO_x jumps dominates at all temperatures, representing 69 % of the oxide ion jumps at 200 °C, but decreasing to 56 % of jumps at 600 °C as the other events become more frequent. The proportion of jumps attributed to movement within the Bi-O sublattice (long-range diffusional motion) represents a significant portion of the total jumps. However, it is important to note that at any one time significantly fewer oxygen atoms are within the V-O sublattice than in the Bi-O sublattice (initially 36 and 135 O atoms, respectively). This means the intra-VO_x jumps are all attributable to only ≈ 21 % of the oxygen atoms and that, per atom, fewer than one Bi-O jump occurs for every ≈ 9 intra-VO_x jumps at 200 °C. This is consistent with the proposal that the intra-VO_x process occurs much faster than the Bi-O sublattice process.

The number of jumps between the Bi-O sublattice and the VO_x coordination spheres and *vice versa* is low at all temperatures in comparison to the two main mechanisms, although the proportion does increase slightly with temperature (to 11% at 600°C). The exchanges of oxide ions between the two sublattices manifest themselves in the variation of the average coordination number of the V atoms over the course of the simulations at each temperature (Figure S4). The oxide ion exchanges between the two sublattices simulated here have been observed experimentally by variable temperature ^{17}O solid state NMR, which showed a clear coalescence of the signals from the two sublattices. [40]

Our results indicate that oxide conduction in $Bi_{0.913}V_{0.087}O_{1.587}$ proceeds by two main processes, each within one of the two sublattices in the structure, but that these are facilitated by O^{2-} exchanges between the two. The first is a slower process through the Bi-O sublattice. At elevated temperatures, this mechanism is mainly responsible for the long-range conduction in the material and involves oxide ion jumps from one site in the Bi-O sublattice to an adjacent vacant site (Figure S5b, cf. Figure S5a which depicts localised thermal vibrations of the same atoms at 200 °C). This movement involves jumps between the nearest-neighbour oxygen sites *via* octahedral holes in the pseudo-cubic structure, and matches with the established conduction pathway in δ-Bi_2O_3.[45,46] The second process is the rapid movement of oxygen atoms within a VO_x group. At low temperatures the displacement clouds are centred on the oxygen sites (Figure S5c); there is some overlap, showing that movement between these sites is possible even at 200 °C. At the higher temperatures the displacement cloud is effectively spherical (Figure S5d), indicating that the individual oxygens are highly delocalised within the V coordination sphere. While this mechanism represents localised intra-VO_x motions, and so does not contribute directly to the long range dynamics in the material, it provides a way to indirectly aid conductivity through the exchanges of the O^{2-} ions between the V-O and the Bi-O sublattices.

Conclusions

Quasielastic neutron scattering measurements have been used to directly observe oxide ion dynamics on the nanosecond time-scale in the oxide ion conductor $Bi_{0.913}V_{0.087}O_{1.587}$. This is the longest timescale neutron scattering study of any fluorite-type solid electrolyte. In addition, it represents only the second case of oxide ion dynamics in a solid electrolyte observed on a nanosecond timescale by quasielastic neutron scattering.

The AIMD simulations reveal two processes that contribute to the oxide ion dynamics in the material. One of these, the long-range diffusive movement of oxide ions through the Bi-O sublattice, is a slower process for which AIMD gives an activation energy of 0.38(2) eV, in agreement with the QENS measurements (0.39(4) eV), indicating that these simulations are reliable and that the QENS indeed probed this long-range diffusive process. The second process is the mainly localised motion of oxygen atoms within the VO_x groups in the material. This volume-constrained dynamics could not be detected directly by QENS. This process is faster than the first, but does not directly contribute to the long range conduction. Instead, it facilitates the movement of oxygen atoms into and out of the VO_x groups and, owing to the flexible coordination requirements of the V^{5+} cation, allows the VO_4 groups to accept additional oxygens atoms from the Bi-O sublattice. This creates additional vacancies in the Bi-O sublattice, further facilitating conduction *via* the first process. The length of the trajectories accessed by *ab initio* simulations and the validation of the simulations by neutron scattering experiments give the first quantitative insight into the relative contributions of the two processes to the oxide ion conduction in this remarkable solid electrolyte.

Finally, this quantitative insight can be used to propose design principles for chemical modifications of this material to improve its properties further. For example, aliovalent doping may be used to generate more vacancies in the Bi-O sublattice in the as-synthesised material; also, slightly V-richer compositions could be prepared to provide more VO_4 groups, which would accept additional oxide ions at elevated temperatures and create more vacancies in the Bi-O sublattice, thus promoting the main long-range diffusion mechanism. It should be noted that $Bi_{0.913}V_{0.087}O_{1.587}$ is already an exceptional oxide ion conductor in the so-called low-temperature SOFC (LT-SOFC) region. At these temperatures engineering solutions (use of heterostructures and bilayer electrolytes[47]) can be expected to alleviate the problems related to the reducibility at the anode that has historically hindered the use of Bi(III)-based electrolytes in high-temperatures SOFCs.

ASSOCIATED CONTENT

Supporting Information. Additional figures related to the analysis of the neutron scattering data and AIMD simulations are available free of charge via the Internet at http://pubs.acs.org.

AUTHOR INFORMATION

Corresponding Authors

*I. Radosavljevic Evans: ivana.radosavljevic@durham.ac.uk, and A. Piovano: piovano@ill.fr

ACKNOWLEDGEMENT

The authors thank Durham University and Institut Laue Langevin for a PhD studentship for J. R. P., Institut Laue Langevin for a summer research studentship for C. A. F, and the Royal Society and the Leverhulme Trust for the award of a Senior Research Fellowship (SRF\R1\180040) to I. R. E.

REFERENCES

(1) Steele, B. C. H.; Heinzel, A. *Nature* **2001**, *414*, 345.
(2) Goodenough, J. B. *Ann.l Rev. Mater. Res.* **2003**, *33*, 91.
(3) Knauth, P.; Tuller, H. L. *J. Amer. Ceram. Soc.* **2002**, *85*, 1654.
(4) Ramamoorthy, R.; Dutta, P. K.; Akbar, S. A. *J. Mat. Sci.* **2003**, *38*, 4271.
(5) Lashtabeg, A.; Skinner, S. J. *J. Mat. Chem.* **2006**, *16*, 3161.
(6) Brett, D. J. L.; Atkinson, A.; Brandon, N. P.; Skinner, S. J. *Chem. Soc. Rev.* **2008**, *37*, 1568.
(7) Kuang, X.; Payne, J. L.; Johnson, M. R.; Evans, I. R. *Angew. Chem. Int. Edit.* **2012**, *51*, 690.
(8) Kuang, X.; Payne, J. L.; Farrell, J. D.; Johnson, M. R.; Evans, I. R. *Chem. Mater.* **2012**, *24*, 2162.
(9) Ling, C. D.; Miiler, W.; Johnson, M. R.; Richard, D.; Rols, S.; Madge, J.; Evans, I. R. *Chem. Mater.* **2012**, *24*, 4607.
(10) Payne, J. L.; Farrell, J. D.; Linsell, A. M.; Johnson, M. R.; Evans, I. R. *Solid State Ion.* **2013**, *244*, 35.
(11) Tate, M. L.; Hack, J.; Kuang, X.; McIntyre, G. J.; Withers, R. L.; Johnson, M. R.; Radosavljevic Evans, I. *J. Solid State Chem.* **2015**, *225*, 383.
(12) Hempelman, R. *Quasielastic Neutron Scattering and Solid State Diffusion*; Oxford University Press, 2000; Vol. 13.
(13) Karlsson, M. *Phys. Chem. Chem. Phys.* **2015**, *17*, 26.
(14) Mamontov, E. *Solid State Ion.* **2016**, *296*, 158.
(15) Wind, J.; Mole, R.; Yu, D.; Ling, C. *Chem. Mater.* **2017**, *29*, 7408.
(16) Peet, J. R.; Fuller, C. A.; Frick, B.; Zbiri, M.; Piovano, A.; Johnson, M. R.; Evans, I. R. *Chem. Mater.* **2017**, *29*, 3020.
(17) Evans, I. R.; Howard, J. A. K.; Evans, J. S. O. *Chem. Mater.* **2005**, *17*, 4074.
(18) Peet, J. R.; Chambers, M. S.; Piovano, A.; Johnson, M. R.; Evans, I. R. *J. Mat. Chem. A* **2018**, *6*, 5129.
(19) Coelho, A. A.; Evans, J. S. O.; Evans, I. R.; Kern, A.; Parsons, S. *Powder Diffraction* **2011**, *26*, S22.
(20) Dinnebier Robert, E.; Leineweber, A.; Evans John, S. O. *Rietveld Refinement, Practical Powder Diffraction Pattern Analysis using TOPAS*, 2018.
(21) Rietveld, H. M. *J. Appl. Cryst.* **1969**, *2*, 65.
(22) Frick, B.; Combet, J.; van Eijck, L. *Nucl. Instrum. Methods Phys. Res. Sect. A-Accel. Spectrom. Dect. Assoc. Equip.* **2012**, *669*, 7.
(23) Richard, D.; Ferrand, M.; G.; Kearley, J. *J. Neutron Res.* **1996**, *4*, 33.
(24) Kresse, G.; Furthmuller, J. *Comp. Mater. Sci.* **1996**, *6*, 15.
(25) Kresse, G.; Joubert, D. *Phys. Rev. B* **1999**, *59*, 1758.
(26) Perdew, J.; Burke, K.; Ernzerhof, M. *Phys. Rev. Lett.* **1996**, *77*, 3865.
(27) Pellegrini, E. C.; Goret, G.; Aoun, A. **2016**.
(28) Chudley, C. T.; Elliott, R. J. *Proc. Phys. Soc. London* **1961**, *77*, 353.
(29) Wilmer, D.; Feldmann, H.; Lechner, R. E. *Phys. Chem. Chem. Phys.* **2002**, *4*, 3260.

(30) Wilmer, D.; Funke, K.; Witschas, M.; Banhatti, R. D.; Jansen, M.; Korus, G.; Fitter, J.; Lechner, R. E. *Physica B* **1999**, *266*, 60.
(31) Peet, J. R.; Widdifield, C. M.; Apperley, D. C.; Hodgkinson, P.; Johnson, M. R.; Evans, I. R. *Chem. Commun.* **2015**, *51*, 17163.
(32) Kim, N.; Hsieh, C.; Huang, H.; Prinz, F.; Stebbins, J. *Solid State Ion.* **2007**, *178*, 1499.
(33) Fuda, K.; Kishio, K.; Yamauchi, S.; Fueki, K.; Onoda, Y. *J. Phys. Chem. Solids* **1984**, *45*, 1253.
(34) Yamada, K.; Kumano, K.; Okuda, T. *Solid State Ion.* **2005**, *176*, 823.
(35) Udovic, T.; Matsuo, M.; Tang, W.; Wu, H.; Stavila, V.; Soloninin, A.; Skoryunov, R.; Babanova, O.; Skripov, A.; Rush, J.; Unemoto, A.; Takamura, H.; Orimo, S. *Adv. Mater.* **2014**, *26*, 7622.
(36) Santibáñez-Mendieta, A. B.; Didier, C.; Inglis, K. K.; Corkett, A. J.; Pitcher, M. J.; Zanella, M.; Shin, J. F.; Daniels, L. M.; Rakhmatullin, A.; Li, M.; Dyer, M. S.; Claridge, J. B.; Blanc, F.; Rosseinsky, M. J. *Chem. Mater.* **2016**, *28*, 7833.
(37) Arbi, K.; Lazarraga, M.; Chehimi, D.; Ayadi-Trabelsi, M.; Rojo, J.; Sanz, J. *Chem. Mater.* **2004**, *16*, 255.
(38) Moreno, K. J.; Mendoza-Suarez, G.; Fuentes, A. F.; Garcia-Barriocanal, J.; Leon, C.; Santamaria, J. *Phys. Rev. B* **2005**, *71*, 4.
(39) Ngai, K. L.; Santamaria, J.; Leon, C. *Eur. Phys. J. B* **2013**, *86*, 10.
(40) Dunstan, M. T.; Halat, D. M.; Tate, M. L.; Evans, I. R.; Grey, C. P. *Chem. Mater.* **2019**, *31*, 1704.
(41) Allen, S.; Evans, J. S. O. *J. Mat. Chem.* **2004**, *14*, 151.
(42) Evans, J. S. O.; Hanson, P. A.; Ibberson, R. M.; Duan, N.; Kameswari, U.; Sleight, A. W. *J. Amer. Chem. Soc.* **2000**, *122*, 8694.
(43) Hampson, M. R.; Evans, J. S. O.; Hodgkinson, P. *J. Amer. Chem. Soc.* **2005**, *127*, 15175.
(44) Jakobsen, H. J.; Bildsoe, H.; Brorson, M.; Gan, Z. H.; Hung, I. *J. Phys. Chem. C* **2014**, *118*, 20639.
(45) Goodenough, J. B. *Annu. Rev. Mater. Res.* **2003**, *33*, 91.
(46) Boyapati, S.; Wachsman, E. D.; Chakoumakos, B. C. *Solid State Ion.* **2001**, *138*, 293.
(47) Wachsman, E. D.; Lee, K. T. *Science* **2011**, *334*, 935.

Table of Contents artwork